IOP Publishing | Astro Ltd Laser Physics
Laser Phys. **34** (2024) 045602 (15pp) https://doi.org/10.1088/1555-6611/ad26ea

Hybrid modeling and optimization of fiber laser hole cutting of austenitic stainless-steel sheets using response surface

Zhenhua Niu[1,*], Mohammad Hossein Razavi Dehkordi[2,3], Mohammadreza Ghazi[2] and Mohammad Akbari[2,3,*]

[1] College of Electromechanical Engineering, Anyang Vocational and Technical College, AnYang 455000, People's Republic of China
[2] Department of Mechanical Engineering, Najafabad Branch, Islamic Azad University, Najafabad, Iran
[3] Aerospace and Energy Conversion Research Center, Najafabad Branch, Islamic Azad University, Najafabad, Iran

E-mail: ayzyjd007@sina.com and m.akbari.g80@gmail.com

Abstract

In this study, an efficient approach was proposed to systematically model and optimize the laser small hole cutting process parameters using a hybrid approach for the design of experiment and multi-objective genetic algorithm optimization. The central composite design and response surface methodology were used to effectively model the impact of four main factors: cutting speed, laser power, gas pressure and focal distance on the responses. The responses considered were hole diameter circularity tolerance, spattering and cut kerf width, which were used to evaluate the quality of the laser hole cutting. The regression equations were used to model the effect of process parameters and their interactions on the responses. These regression models were then used as objective functions for optimization. The results show that the focal distance and laser power have had a significant influence on the hole diameter circularity tolerance and the variation in size of the cut kerf. In particular, the melted material spattering rate increased threefold when the focal distance increased from 0.4 to 0.8 mm. The optimization results highlighted that the best outcomes in terms of minimum deviation, spatter, and the cut-kerf width were achieved at low power (between 605 and 685 W) and low speeds (in the range of 11.1–12.7 m min^{-1}). The optimal focal distance for all solutions was found to be 0 mm for the gas pressure (between 6.5 and 8 bars) to minimize the objective functions.

Keywords: laser hole cutting, response surface methodology, multi-objective genetic algorithm, dimensional tolerances, optimization

1. Introduction

Fiber laser technology has drastically revolutionized the way that metal is produced, delivering significant improvements over conventional cutting and drilling procedures. There has been significant interest in fiber laser hole drilling in stainless steel because of its accuracy, speed and affordability. In addition, machine learning [1, 2], artificial intelligence and numerical approaches are now widely used in various industries [3–7]. To achieve the greatest results in fiber laser hole drilling, reliable models and efficient optimization techniques must

* Authors to whom any correspondence should be addressed.

be developed. Through modeling, we are able to understand the complex relationships that exist between laser parameters, material properties and process conditions. Conversely, optimization allows us to ascertain the optimal combination of variables to achieve targeted outcomes such as enhanced hole quality, heightened production and reduced expenses. To model fiber laser hole drilling, the physical events that occur during the process must be represented mathematically. Material removal, melt ejection, melt transfer and laser beam absorption are some of these occurrences. By building precise models, scientists and engineers can forecast process outcomes, simulate laser-material interactions and optimize parameter settings. Optimization strategies lead to increased efficiency and effectiveness in fiber laser hole drilling and cutting. These algorithms systematically search the parameter space to determine the optimal ratio of laser power, pulse duration, focal position, gas pressure and scanning speed [8]. The objective is to minimize expenses and material waste while optimizing process performance metrics such as hole quality, productivity and energy efficiency. Advanced methods, including genetic algorithms, simulated annealing, artificial neural network (ANN), response surface method (RSM) [9] and particle swarm optimization [10] are frequently used in the optimization process [11, 12]. These techniques take into consideration different goals and limits and enable the study of a large parameter space. By continuously experimenting with different parameter combinations, the optimization approach aims to find the global optimum and guarantee the best results for fiber laser hole drilling in stainless steel. As a result, modeling and optimization of stainless steel fiber laser holes are necessary to improve the process performance. Scientists and engineers can increase hole quality, productivity and economy of cost by careful modeling of the interaction between laser and material and careful exploration of the parameter space [13]. These advancements in modeling and optimization techniques support the ongoing development of fiber laser technology and its use in metal processing. Researchers have conducted investigations in this area. The temperature effects of laser drilling on mechanical parameters and drilling quality were studied by Li *et al* [14] The results demonstrated that excessive damage lowers the tensile and bending strength of carbon fiber-reinforced plastic and aggravates fatigue crack propagation. In addition, Taguchi grey relational analysis-based laser beam drilling process optimization during Inconel alloy machining was studied by Alsoruji *et al* [15]. After evaluating the factors influencing the quality of the drilling, it was discovered that gas pressure—which is crucial for focused energy—plays a significant part in the operation. The optimization of surface quality monitoring in titanium alloy machining during the laser drilling process was studied by Muthuramalingam *et al* [16]. The results show that surface roughness can be reduced by increasing laser power and decreasing the nozzle distance. This is because smaller craters with lower particle adhesion form. Using the grey relational analysis approach, Chengal Reddy *et al* [17] determined the ideal laser settings during the laser drilling process of Alloy 303. The analysis of variance data show that the pulse frequency parameter is the one that has the biggest impact on how well the laser drilling process works. Gopinath *et al's* [18] study used parameters optimized by the technique for order preference based on similarity to the ideal solution approach to examine the quality of laser cutting for cutting duplex steel. Their findings demonstrate that, in comparison to the original trails, a higher surface quality may be attained by employing the discovered optimal values. With the use of ANNs, Chatterjee *et al* [19] assessed the drilling quality produced by the Ray laser drilling technique. Multi-gene genetic programming models outperform adaptive neuro-fuzzy inference system models in their ability to forecast performance criteria during laser drilling operations. Pramanik *et al*'s [20] investigation used suitable parameters derived from the RSM to examine the low-power fiber laser cutting capabilities on AISI 316 L stainless steel. Their findings demonstrate that the quality of the cutting edge might be raised by selecting the most suitable and ideal parameters for the procedure. The effects of assist gas pressure, laser pulse energy and ultrasonic vibrations on the laser drilling process were examined by Xia *et al* [21] Their findings demonstrate that selecting the appropriate drilling parameters can improve the quality of the cutting surface. In a laser drilling procedure on magnesium alloys, Wang *et al* [22] examined cutting quality both with and without submersion in water. Their findings show that the cooling-insulating properties of water significantly lessen residue development and recast layer generation. Hüseyin *et al* [23] investigated hole formation during laser drilling of ferritic stainless steel and presented a mathematical model for burr height. By analyzing the variance, the results showed that the most important parameter for the hole height is the feeding speed. A two-step approach has been developed by Wang *et al* [24] to improve the quality of laser drilling of thermal barrier coated nickel-based alloys. By comparing their results with experimental results, the validity of this two-step approach is confirmed, and ultimately high-quality drilled holes are obtained. Amaral *et al* [25] increased the quality of the final product by optimizing parameters in the fiber laser cutting process. Their results indicate that by choosing a higher cutting speed, the quality of the cutting surface can be increased and an optimal process can be identified. Ay [26] looked into the quality of the laser drilling process when drilling into Ti–6Al–4V alloy. The results show that the extreme learning machine approach outperforms the ANN technique in terms of performance and error margin. It also operates more quickly. Moradi and Golchin [27] used the finite element technique to study the factors that impact laser drilling. The inlet and outlet diameters of the holes, the taper angle, and the weight of the mass evacuated from the hole all clearly increased with an increase in the laser input process parameters, according to a comparison of the experimental and numerical data.

In order to accurately model the impact of laser cutting process parameters on hole dimensional tolerances and cut quality in terms of spattering and cut kerf width using central composite design (CCD) and RSM, this study examines

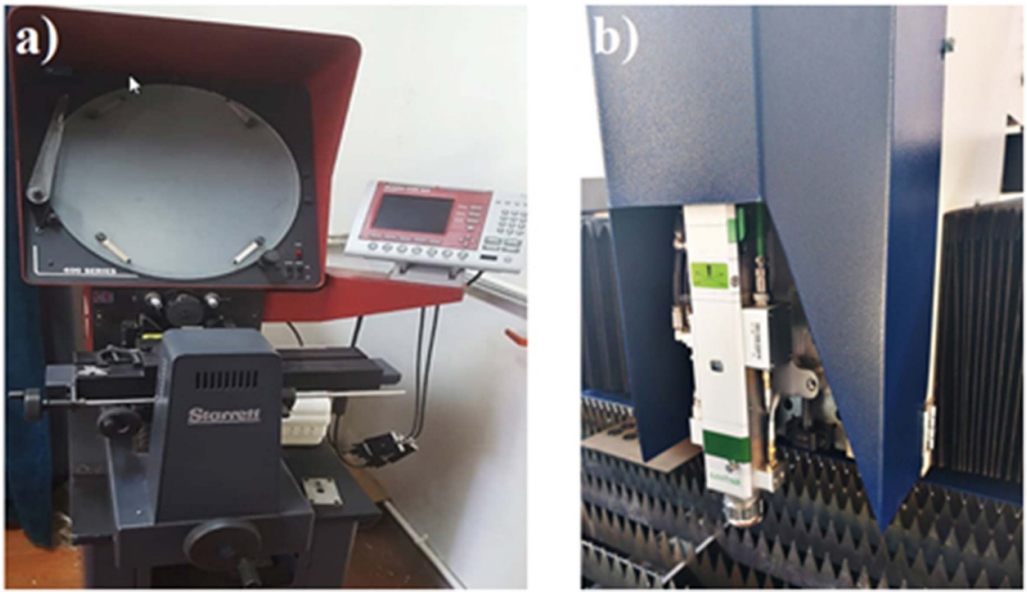

Figure 1. Devices used for the experiments: (a) comparator, (b) laser cutting machine.

Table 1. Experimental test condition.

Row No.	Power (W)	Speed (m min^{-1})	Focal distance (mm)	Pressure (bar)
1	1000	10	0.5	6
2	900	12	0.8	8
3	700	16	0.2	5
4	600	5	0.2	7
5	500	6	0.5	6

the laser small hole cutting process through the design of experiments (DOEs). In addition, a multi-objective genetic algorithm (MOGA) was created to optimize the process parameters in order to minimize spattering and dimensional tolerances. Compared to forecasting the answers using a neural network, the response surface approach allows for an accurate modeling of the influence of laser hole cutting process parameters using a small number of tests. This paper uses a unique technique by modeling the replies using RSM and integrating a multi-objective evolutionary algorithm for more efficient optimization than statistical optimization. With less time and money spent, this hybrid technique can efficiently simulate and optimize laser hole cutting.

2. Laser hole cutting experiments

A detailed description of the materials, equipment and experimental conditions are presented to address the laser hole cutting process more comprehensively.

2.1. Materials and methods

A 3-axis fiber laser cutting CNC machine with maximum output power of 1500 W was used for the experiments. The laser source was equipped with a Raytools autofocus BM109 cutting head. Purified oxygen gas with a purity of 99% was applied at a maximum pressure of 8 MPa through a single nozzle. The material used for the experiments was 304 stainless steel with a thickness of 0.8 mm. To provide images of the hole, a scanning electron microscope was used. A Starrett HB400 optical comparator was used for non-contact measurement of the hole diameter at different positions. Images of the comparator and laser cutting CNC used in this study are shown in figure 1. An Olympus SZX-18 stereoscope was used to visually check the condition of the holes.

2.2. Laser hole cutting DOE

Laser hole cutting experiments were conducted using DOE methods to systematically evaluate the effect of the laser process parameters on cut quality and dimensional tolerances in order to optimize the process parameters. Based on the initial experiments shown in table 1, the basic selection of parameter levels was determined to assess the levels of cutting parameters. The piercing parameters, such as pierce time, pierce frequency and peak power, were initially evaluated primarily to reach an acceptable level for cutting experiments. Subsequently, the main levels of the experiments were selected.

Table 2 and figure 2 illustrate the procedure for selecting the appropriate piercing parameters. Selection of the parameter

Table 2. Piercing test condition at cutting speed of 12 m min^{-1}, laser power of 700 W and pressure of 6 bar at a focal distance of 0.5 mm.

Row No.	Peak power (W)	Pressure (bar)	Duty cycle (%)	Pulse frequency (Hz)
1	1500	6	90	1000
2	1200	7	100	1500
3	1000	5	100	3000
4	1000	4	85	4000
5	1200	3	100	2000

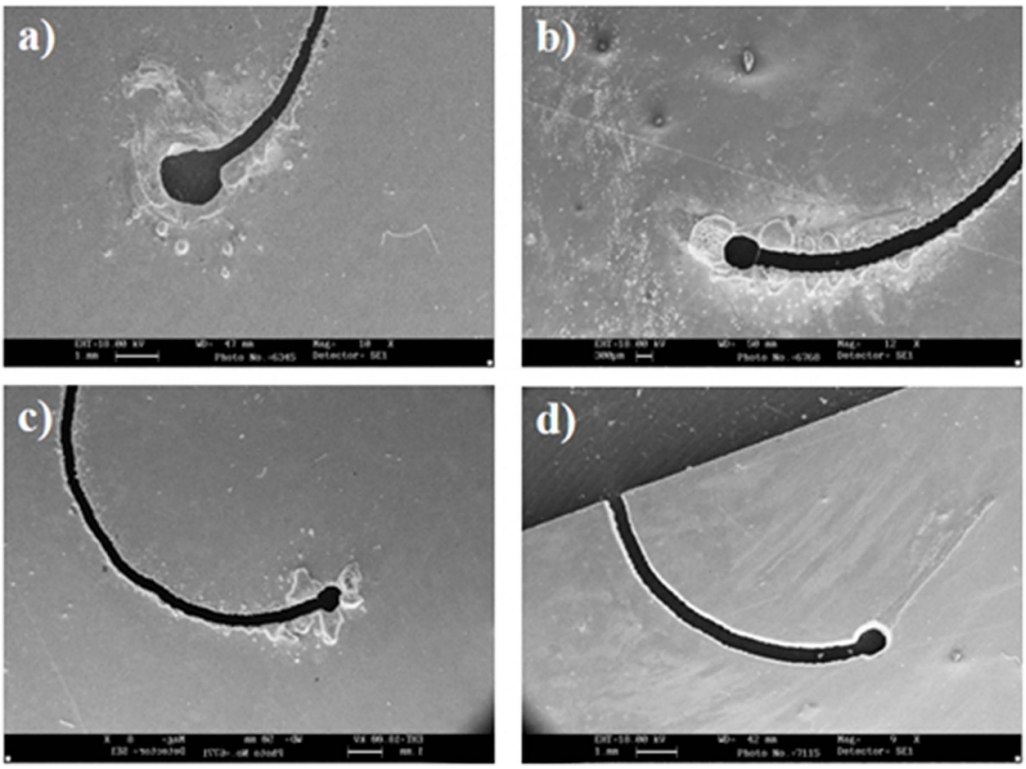

Figure 2. Effect of piercing parameters from table 2 for experiments (a) 5, (b) 2, (c) 4, (d) 3.

levels was determined through CCD and RSM based on preliminary experiments. The experiments were designed to examine the impact of four cutting process factors (laser power, cutting speed, focal distance and gas pressure) on three responses including hole diameter deviation, cut kerf width and spattering.

As can be observed in table 3, a total of 29 experiments were conducted. The designed matrix consisted of five points in the center, eight axial points and 16 cubic points. The independent variables of these experiments were the cutting speed, laser power, focal distance and gas pressure. The cutting speed was chosen between 12 and 16 m min^{-1}, the power range was from 700 to 1000 W, the focal distance varied between 0 and 1.1 mm and the gas pressure ranged from 5–7 bar. The purpose of the DOE was to evaluate the impact of the laser cutting parameters on the variation of the responses. The responses were measured in terms of hole deviation, cut kerf width and amount of spattering, as shown in figure 3.

3. Results and discussion

This section presents the experimental results based on the CCD experiments. The effects of the parameters and their interactions on the responses are presented.

3.1. Effect of laser process parameters on hole cutting quality

Based on the experimental results of the laser cutting, a comprehensive investigation was conducted to analyze the effect of each factor including linear and square terms as well as their interaction on the responses.

3.1.1. Effect of laser parameters on hole deviation. The effect of laser cutting process parameters on hole diameter deviation is investigated. Table 4 shows the analysis of variance (ANOVA) results, which clearly imply that the

Table 3. Data matrix for laser hole cutting based on CCD.

	Input date				Response		
Row No.	Power (W)	Speed (m min^{-1})	Focal distance (mm)	Pressure (bar)	Deviation (mm)	Spatter (%)	Cut-kerf width (mm)
1	1000	14	0.5	6	0.226	25	0.238
2	900	12	0.8	5	0.228	30	0.242
3	900	16	0.2	5	0.219	18	0.202
4	900	12	0.2	7	0.216	18	0.182
5	800	14	0.5	6	0.214	17	0.203
6	800	14	0.5	6	0.205	12	0.192
7	900	16	0.2	7	0.215	20	0.185
8	700	16	0.2	7	0.204	15	0.178
9	900	12	0.2	5	0.215	21	0.207
10	800	14	0.5	6	0.216	10	0.188
11	800	14	0.5	6	0.208	8	0.212
12	700	12	0.2	5	0.189	2	0.192
13	800	14	0.5	8	0.196	13	0.223
14	800	14	−0.1	6	0.188	4	0.187
15	700	16	0.2	5	0.214	17	0.188
16	700	16	0.8	7	0.236	39	0.226
17	700	12	0.8	5	0.234	35	0.216
18	600	14	0.5	6	0.216	14	0.195
19	800	14	0.5	6	0.211	15	0.182
20	900	12	0.8	7	0.234	34	0.232
21	800	14	1.1	6	0.234	48	0.251
22	700	16	0.8	5	0.233	27	0.194
23	800	10	0.5	6	0.227	18	0.215
24	700	12	0.8	7	0.226	24	0.221
25	900	16	0.8	5	0.238	38	0.231
26	700	12	0.2	7	0.185	5	0.183
27	800	18	0.5	6	0.228	26	0.187
28	800	14	0.5	4	0.209	23	0.198
29	900	16	0.8	7	0.228	41	0.264

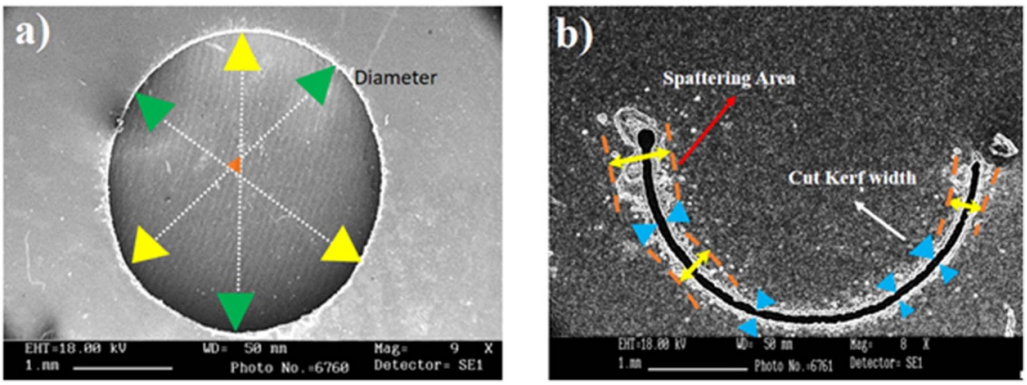

Figure 3. Measurement methods for (a) hole diameter deviation, (b) cut kerf width and spattering.

regression model is in appropriate agreement with the experimental data with R-square of 85.9% and lack of fit 0.43. The linear terms of focal distance and laser power have had a significant influence on hole diameter. Furthermore, the interaction of laser power and focal distance, as well as the square of speed, had a remarkable effect on hole diameter deviation. The regression equation (1) shows the linear and interaction terms between process parameters and deviation:

$$\begin{aligned}\text{Deviation (mm)} = {} & 0.172 + 0.000115\ \text{power} - 0.0237\text{speed} \\ & + 0.2021\ \text{focal distance} + 0.0280\ \text{pressure} \\ & + 0.001062\ \text{speed} \times \text{speed} + 0.0014\ \text{focal distance} \\ & \times \text{focal distance} - 0.00200\ \text{pressure} \times \text{pressure} \\ & - 0.000154\ \text{power} \times \text{focal distance} - 0.00354\ \text{speed} \\ & \times \text{focal distance} - 0.000500\ \text{speed} \times \text{pressure} \\ & + 0.00167\ \text{focal distance} \times \text{pressure}. \end{aligned} \quad (1)$$

Table 4. The result of ANOVA for hole diameter deviation.

Source	DF	Adj SS	Adj MS	F-Value	P-Value
Model	11	0.005297	0.000482	9.41	0.000
Linear	4	0.004178	0.001045	20.42	0.000
Power	1	0.000353	0.000353	6.89	0.018
Speed	1	0.000160	0.000160	3.13	0.095
Focal distance	1	0.003553	0.003553	69.45	0.000
Pressure	1	0.000113	0.000113	2.20	0.156
Square	3	0.000685	0.000228	4.46	0.017
Speed × speed	1	0.000486	0.000486	9.50	0.007
Focal distance × focal distance	1	0.000000	0.000000	0.01	0.929
Pressure × pressure	1	0.000108	0.000108	2.10	0.165
2-way interaction	4	0.000435	0.000109	2.12	0.122
Power × focal distance	1	0.000342	0.000342	6.69	0.019
Speed × focal distance	1	0.000072	0.000072	1.41	0.251
Speed × pressure	1	0.000016	0.000016	0.31	0.583
Focal distance × pressure	1	0.000004	0.000004	0.08	0.783
Error	17	0.000870	0.000051		
Lack of fit	13	0.000791	0.000061	3.09	0.143
Pure error	4	0.000079	0.000020		
Total	28	0.006167			

S	R-square	R-square(adj)	R-square(pred)
0.0071521	85.90%	76.78%	53.77%

With the increase in laser power from 600 W, the number of dimensional changes in the hole diameter continually increases. However, this effect remains the same at different speeds. Increasing laser power beyond 600 W results in more heating and further dimensional changes. Figure 4(a) depicts that at a speed of 10 m min^{-1}, due to the low speed and the creation of a high temperature gradient, as well as a larger melt volume in the narrow cut kerf area, the dimensional deviation in the hole diameter was approximately 0.02 mm. Within the selected power range of 600–1050 W, the minimum deviation was observed at a cutting speed of 13 m min^{-1}. Hence, it can be concluded that laser power below 750 W and speed around 13 m min^{-1} could result in the minimum deviation.

Due to the lack of continuity and uniformity in the flow of the molten particles exiting from the bottom part of the cut kerf area, there are greater dimensional changes when cutting at a speed of 10 m min^{-1} compared to 13 m min^{-1}. Increasing the cutting speed to 17 m min^{-1}, further increases the changes in the cut kerf from 0.2 to 0.24 mm, which represents about 20% augmentation in dimensional changes. The insufficient exit of the molten material from the cut kerf leads to increased dimensional changes in the hole diameter across different areas due to the discontinuous flow of the melted material and changes in the size of the cut gap area. The smallest deviation of hole diameter occurs when cutting at a speed of 13 m min^{-1} with a power of 600 W.

Figure 4(b) depicts the impact of laser power and focal distance on the dimensional changes of the hole diameter. When the laser power was increased from 600 to 1050 W, while cutting at the focal point, the diameter of the hole in the measured points increased by 0.04 mm.

At a laser power of 600 W, the increase in focal distance results in a 0.08 mm increase in the dimensional changes of the hole diameter, which could be attributed to a decrease in the energy density of the laser beam. Consequently, the reduction in laser energy density and insufficient melting in the cut kerf region results in increased dimensional changes in the hole diameter and cut kerf width. On the other hand, increasing the focal distance at a power level of 1050 W causes fewer changes in the diameter of the hole. This is because the energy density of the beam changes and the conditions for the removal of the melted material have been improved. At a focal distance of 1.1 mm, raising the laser power increases the thermal gradient and energy density of the laser beam. As a result, there is a dimensional change of about 0.02 mm in the hole diameter. The hole cutting at the focal point with a power of 600 W has led to the lowest hole diameter deviation.

Figure 4(c) shows the effect of laser power and gas pressure on the changes in hole diameter dimension. As expected, increasing the laser power created 0.01 mm dimensional differences across the hole diameter regardless of the gas pressure levels. The largest difference in the hole diameter was observed when the gas pressure increased from 4 to 6 bar. Furthermore, increasing the gas pressure from 6 to 8 bar facilitates the smooth exit of the melt flow from the cut kerf and minimizes the dimensional changes in the hole diameter.

Figure 4(d) illustrates the effect of the cutting speed and focal distance on the dimensional changes in the hole diameter. When the laser beam is irradiated at the focal point, increasing the speed reduces the interaction time and hinders the melt from exiting the cut kerf region. Therefore, it can be concluded that the effect of changes in focal distance has the effect of more than three times the cutting speed variation on the dimensional changes in the hole diameter. At the focal distance of 1.1 mm, increasing the cutting speed decreased the dimensional changes of the molten pool. This is attributed to

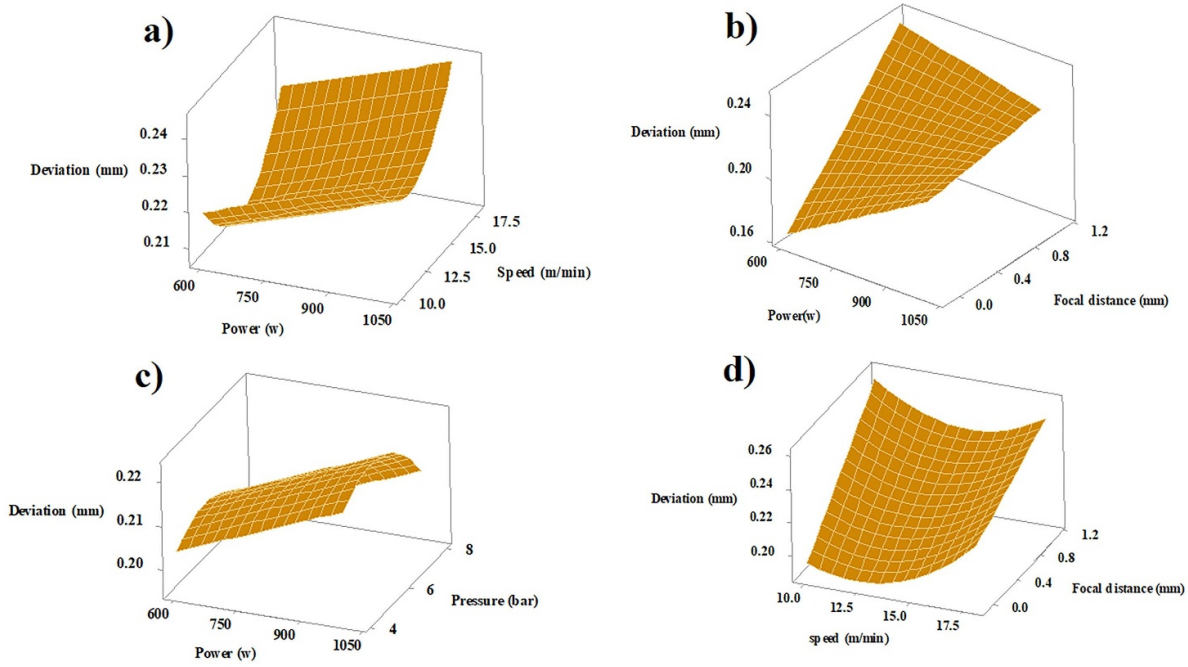

Figure 4. Effect of laser process parameters on hole deviation for (a) power and speed, (b) power and focal distance, (c) power and pressure, (d) speed and focal distance.

Table 5. The result of ANOVA for cut kerf.

Source	DF	Adj SS	Adj MS	F-Value	P-Value
Model	11	0.012807	0.001164	8.60	0.000
Linear	4	0.010484	0.002621	19.36	0.000
Power	1	0.002262	0.002262	16.71	0.001
Speed	1	0.000165	0.000165	1.22	0.284
Focal distance	1	0.007957	0.007957	58.76	0.000
Pressure	1	0.000100	0.000100	0.74	0.402
Square	3	0.000652	0.000217	1.61	0.225
Speed × speed	1	0.000000	0.000000	0.00	0.992
Focal distance × focal distance	1	0.000550	0.000550	4.06	0.060
Pressure × pressure	1	0.000155	0.000155	1.14	0.300
2-way interaction	4	0.001670	0.000418	3.08	0.044
Power × focal distance	1	0.000371	0.000371	2.74	0.116
Speed × focal distance	1	0.000014	0.000014	0.10	0.751
Speed × pressure	1	0.000371	0.000371	2.74	0.116
Focal distance × pressure	1	0.000915	0.000915	6.76	0.019
Error	17	0.002302	0.000135		
Lack of fit	13	0.001723	0.000133	0.92	0.599
Pure error	4	0.000579	0.000145		
Total	28	0.015109			

S	R-square	R-square(adj)	R-square(pred)
0.0116365	84.76%	74.91%	58.32%

the shorter interaction time between the laser beam and the increased speed, resulting in a narrower cut kerf width.

3.1.2. Effect of laser process parameters on cut kerf width. As shown in table 5, the focal distance and laser power have the greatest effect on the changes in the size of the cut kerf. The values of R-square = 84.7% and lack of fit = 0.599 indicate that the regression model is in a good agreement with the experimental data. The regression equation (2) demonstrates the relationship between the width of the cut kerf and the parameters of the cutting process, incorporating linear, quadratic and parameter interaction terms:

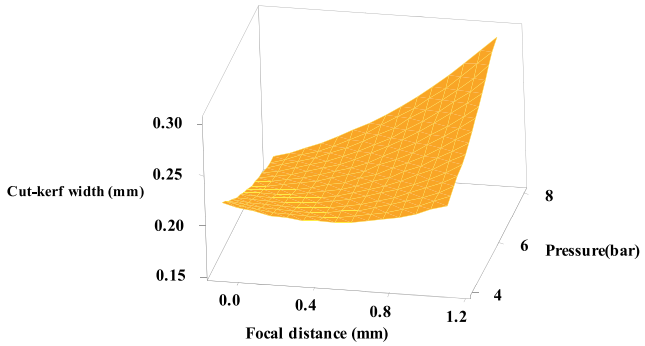

Figure 5. Effect of focal distance and gas pressure on cut kerf width.

$$\begin{aligned}\text{Cut kerf width} = {} & 0.553 + 0.000017\ \text{power} - 0.0167\ \text{speed} \\ & - 0.291\ \text{focal distance} - 0.0730\ \text{pressure} \\ & + 0.000005\ \text{speed} \times \text{speed} + 0.0502\ \text{focal distance} \\ & \times \text{focal distance} + 0.00240\ \text{pressure} \times \text{pressure} \\ & + 0.000160\ \text{power} \times \text{focal distance} + 0.00156\ \text{speed} \\ & \times \text{focaldistance} + 0.00241\ \text{speed} \times \text{pressure} \\ & + 0.02521\ \text{focal distance} \times \text{pressure}. \end{aligned} \quad (2)$$

The effect of focal distance and gas pressure on the changes in the width of the cut kerf can be observed in figure 5. At a pressure of 4 bar, dimensional changes that occur in the cut kerf, due to changes in the focal distance, were about 0.02 mm. The minimum change in the width of the cut kerf occur at the focal point by increasing the focal distance to 1.1 mm; a rise in the gas pressure leads to an increase in the width of the cut kerf up to 0.1 mm. This is about 50% higher than that in the initial state. Therefore, it can be said that by simultaneously increasing the gas pressure to 8 bar and the focal distance to 1.1 mm, the width of the cut kerf has been raised to 0.3 mm.

Figure 6 shows the effect of laser power and focal distance variations on changes in the size of the cut kerf width. At focal distance (0 mm), increasing laser power has had minimal effect on the width of the cut kerf. However, as the focal distance increases, the width of the cut kerf is also raised by 0.1 mm. This increase is due to the larger laser beam diameter, resulting in a higher melting volume of the material and thereby the width of the cut kerf. At a power of 1050 W, the width of the cut kerf reached 0.1 mm. By increasing both the diameter of the laser beam and the laser power, a larger area of the material is melted leading to further increase in the width of the cut kerf up to 0.3 mm.

Figure 7 illustrates the effect of laser power and gas pressure on the width of the cut kerf. As the laser power increases, the width of the cut kerf also increases by 0.03 mm. Conversely, the minimum cut kerf width was obtained at a pressure of 6 bar. When the gas pressure is either reduced or increased, the width of the cut kerf increased due to the inadequate removal of melted material from the cut kerf area. This can cause damage to the cut kerf area. The greatest changes in the width of the cut kerf have occurred at the highest

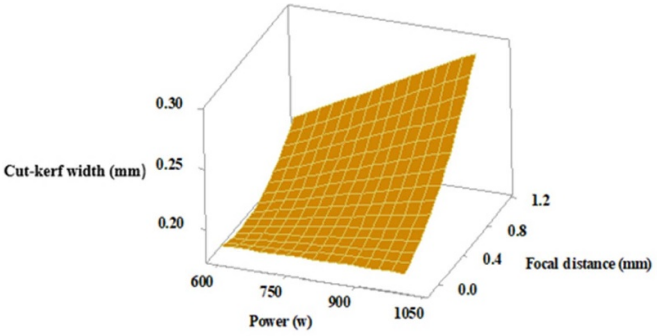

Figure 6. Effect of laser power and focal distance on cut kerf width.

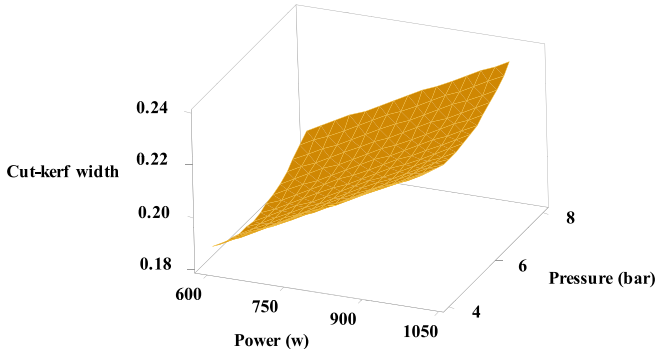

Figure 7. Effect of laser power and focal distance on cut kerf width.

level of laser power as this results in a larger melt volume of melted material in the cut kerf area.

Figure 8 shows the effect of laser power on the variation of cut kerf width. At a laser power of 700 W, the cut kerf width reaches the minimum value with a small amount of spattering and some variation in width, as shown in figure 8(a). At a laser power of 800 W, the optimal cutting condition is achieved, resulting in a smooth cut kerf width with negligible variation and no spattering.

3.1.3. Effect of laser process parameters on spattering. Examining the effect of the hole cutting parameters on the steel sheet reveals that, according to the results obtained from the analysis of variance in table 6, the focal distance and laser power are the two parameters that have the greatest impact on the amount of melt spattering. The R-square 90.28% and lack of fit 0.267 clearly indicate strong agreement between the regression model and data obtained from the experiment.

The regression equation for melt spattering with test parameters is observed in equation (3), which includes linear and quadratic terms as well as the interaction of other working parameters of the process. Figure 9 illustrates the correlation between focal distance and gas pressure in relation to the amount of melt spattering. Increasing the focal distance from 0.4 to 0.8 mm results in a threefold increase in the melt spattering rate. Moreover, the relationship between melt spattering and focal distance is non-linear, exhibiting exponential growth as the focal distance and diameter of the laser beam increases, while the energy density of the laser beam reduces

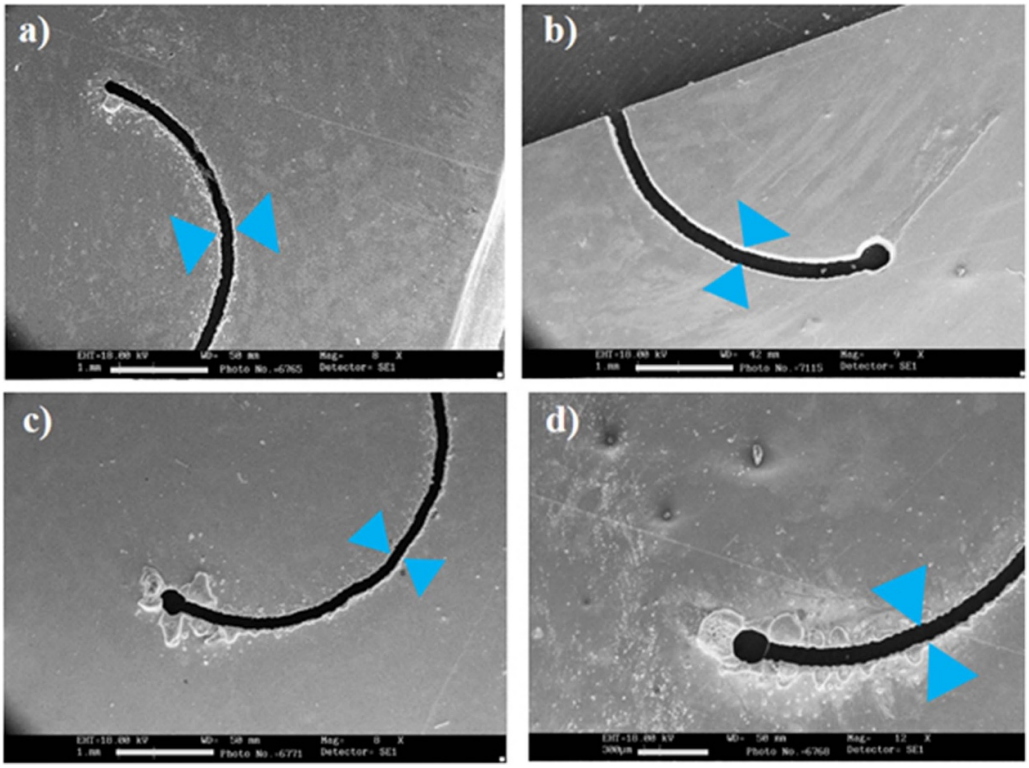

Figure 8. Effect of laser power on cut kerf width at cutting speed of 12 m min^{-1}, gas pressure of 7 bar and laser power of (a) 700 W, (b) 800 W, (c) 900 W, (d) 1000 W.

Table 6. The ANOVA results for spattering.

Source	DF	Adj SS	Adj MS	F-Value	P-Value
Model	12	3428.51	285.71	12.38	0.000
Linear	4	2819.67	704.92	30.54	0.000
Power	1	253.50	253.50	10.98	0.004
Speed	1	160.17	160.17	6.94	0.018
Focal distance	1	2400.00	2400.00	103.99	0.000
Pressure	1	6.00	6.00	0.26	0.617
Square	4	549.34	137.34	5.95	0.004
Power × power	1	127.01	127.01	5.50	0.032
Speed × speed	1	208.90	208.90	9.05	0.008
Focal distance × focal distance	1	382.09	382.09	16.55	0.001
Pressure × pressure	1	87.60	87.60	3.80	0.069
2-way interaction	4	59.50	14.88	0.64	0.639
Power × focal distance	1	25.00	25.00	1.08	0.313
Speed × focal distance	1	0.25	0.25	0.01	0.918
Speed × pressure	1	30.25	30.25	1.31	0.269
Focal distance × pressure	1	4.00	4.00	0.17	0.683
Error	16	369.28	23.08		
Lack of fit	12	316.08	26.34	1.98	0.267
Pure error	4	53.20	13.30		
Total	28	3797.79			

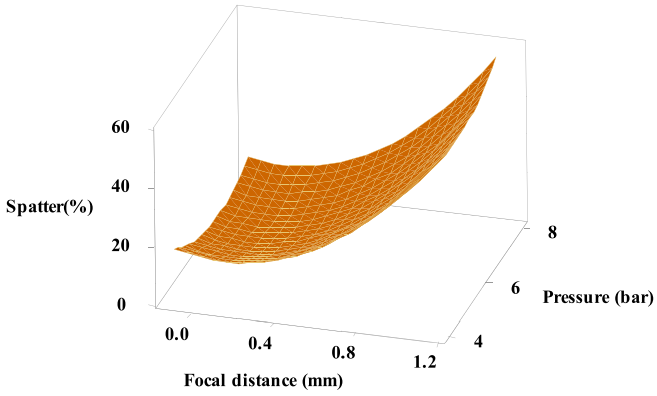

Figure 9. Effect of focal distance and gas pressure on spattering.

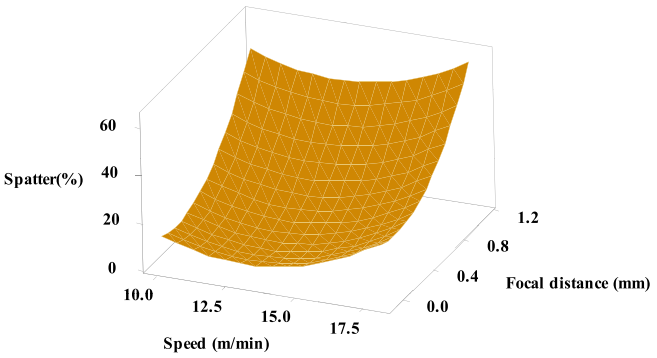

Figure 10. Effect of focal distance and cutting speed on spattering.

$$\begin{aligned}\text{Spattering } (\%) = {} & 357 - 0.301 \text{ power} - 22.59 \text{ speed} \\ & + 16.9 \text{ focal distance} - 33.0 \text{ pressure} + 0.000221 \text{ power} \\ & \times \text{power} + 0.709 \text{ speed} \times \text{speed} + 42.6 \text{ focal distance} \\ & \times \text{focal distance} + 1.837 \text{ pressure} \times \text{pressure} \\ & - 0.0417 \text{ power} \times \text{focal distance} - 0.21 \text{ speed} \\ & \times \text{focal distance} + 0.687 \text{ speed} \times \text{pressure} \\ & + 1.67 \text{ focal distance} \times \text{pressure}. \end{aligned} \quad (3)$$

Due to the increased width of cut kerf in the cutting region and the reduction of the decreased energy density of the laser beam, the melt spattering rate has been exponentially increased. This increase can be attributed to the higher gas pressure, which leads to the creation of more cavitation in the cut kerf area, accumulation of melted materials and inadequate melting rate of the material. On the other hand, the spattering rate was at the lowest level at the focal distance of 0 mm and the gas pressure of 6 bar. The melt spatter rate was at a minimum level of 5%, when cutting at the pressure of 6 bar.

Figure 10 depicts the effect of cutting speed and focal distance on the amount of melt spattering. It can be observed that, by increasing the focal distance, the melt spattering rate was increased to the maximum value of 17 m min^{-1}.

In this case, with the cutting speed increased from 10 to 13 m min^{-1}, the melt spattering rate is diminished by 10%. By further increasing the cutting speed, the melt spattering rate is increased by the same amount. Therefore, it could be said that

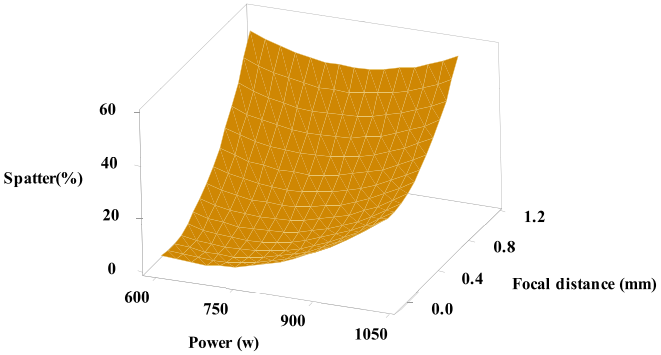

Figure 11. Effect of laser power and focal distance on spattering.

the change in cutting speed from 10 to 13 m min^{-1} results in a decrease in the melt spattering due to the limited melt accumulation in the cut kerf at higher levels of cutting speed. On the other hand, augmentation of the cutting speed from 13 to 17 m min^{-1} causes incomplete cutting and insufficient penetration of the laser in the cut kerf. This causes molten particles to spatter off on the surface instead of exiting from the cut kerf. In addition, at lower cutting speed, the longer reaction time between the laser beam and the surface of the sheet creates a higher melting rate, and the width of the cut kerf causes more melt spattering.

Figure 11 shows the effect of laser power and focal distance on the amount of melt spattering. At the focal point of 0 mm, the melt spattering rate has been raised by about 20% with the increase in laser power. However, with the rise in the focal distance from 0 to 1.1 mm, the melt spattering rate increased by about 60%. It is evident that at the laser power of 600 W, increasing the focal distance causes more melt spattering. Utilizing a lower laser power level and also increasing the focal distance causes a decrease in the energy density of the laser beam. Consequently, incomplete cutting was observed and molten particles spattered and exited from the top of the cut kerf instead of its bottom. (See figure 12).

Therefore, the melt spattering rate is due to insufficient melting in the cut thickness. By increasing the laser power to 750 W, the melt spattering rate decreases. This occurs by increasing the focal distance from 0.4 mm and above. When the laser power is raised to 1050 W, the melt spattering rate increases due to the large melting volume and high melting rate in the cut kerf.

Increasing the focal distance, and thereby enlarging the laser beam diameter, and the increase in laser power lead to an increase in the width of the cut kerf, which creates more melt volume and, as a result, higher level of melt spattering. On the other hand, it can be observed that at the focal point of 0 mm, an increase in laser power always creates a rise in melt spattering.

The lowest melt spattering rate is observed at a power density of 1.9 MW cm^{-2}. Reduction of the laser beam energy density to 0.85 MW cm^{-2} caused an increase in melt spattering of about 60%. In contrast, when the laser beam energy density increases to 1.06 MW cm^{-2}, the melt spattering rate is reduced by 10%. If the laser beam energy density is further

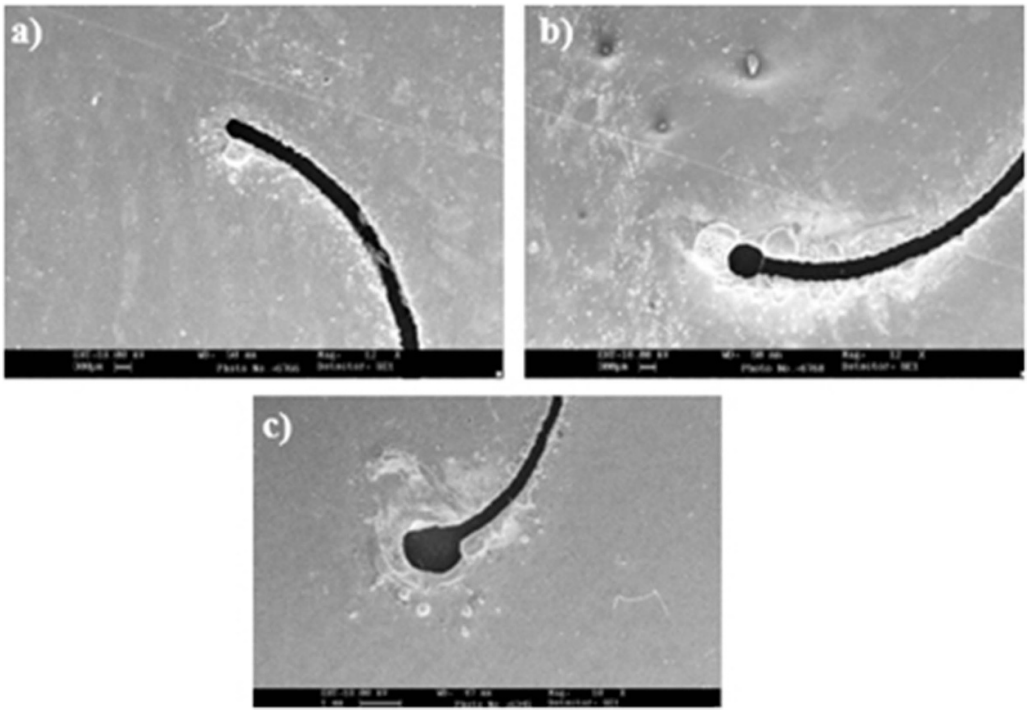

Figure 12. Laser cutting at laser power of 700 W and focal distance of (a) 0.2 mm, (b) 0.8 mm, (c) 1.1 mm.

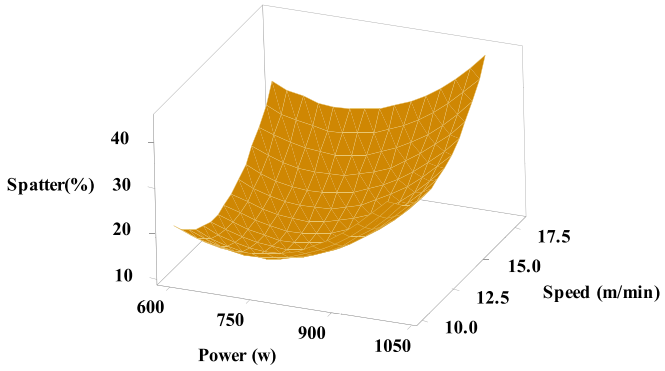

Figure 13. Effect of laser power and cutting speed on spattering.

increased to 21.5 MW cm^{-2}, the melt spattering rate is again raised by 10%. Therefore, it could be said that with laser cutting at the focal point, using energy density between 1.9 and 3.35 MW cm^{-2}, the lowest amount of melt spattering was produced.

When the laser beam energy density is reduced to less than 1.9 MW cm^{-2}, the amount of melt spattering increases. This is due to a larger cut kerf and incomplete melting in the thickness of the sheet.

Figure 13 shows the effect of cutting speed and laser power on the melt spattering rate. Augmentation of the laser power from 600 to 750 W, has increased the melt spattering rate. In addition, at the cutting speed of 10 m min^{-1}, the melt spattering rate was higher than the other speeds. The lowest value of the melt spattering was observed at the speed of 13 m min^{-1}.

Further increase in the cutting speed to 17 m min^{-1} clearly increased the melt spattering rate compared to the speed of 10 m min^{-1}. This is due to insufficient exit of the melt volume and incomplete cut kerf formation from the upper to the lower part of the workpiece. A larger melt volume at lower cutting speed comes out from the lower part of the cut kerf.

3.2. *Multi-objective optimization of laser hole cutting*

3.2.1. Problem description. As mentioned earlier, there are four inputs for the problem: laser power, speed, focal distance and gas pressure. In the conducted experiments, the power ranges from 600–1000 W, the speed varies between 10 and 18 m min^{-1}, the focal distance ranges from 0–1.1 mm, and the pressure was selected between 4 and 8 bar. The outputs are the deviation, spatter and the cut-kerf width. It is desirable to minimize all the outputs so that:

$$\begin{aligned} \text{deviation} &< 0.211\text{mm} \\ \text{spatter} &< 20\% \\ \text{cut - kerf width} &< 0.210\text{mm}. \end{aligned} \tag{4}$$

3.2.2. Method description. The MOGA is an optimization technique inspired by natural evolution and genetic inheritance. It can be used to solve problems with multiple conflicting objectives. The goal of MOGA is to find a set of solutions, known as the Pareto-optimal front, that represents the best trade-offs among the different objectives. By exploring the Pareto-optimal front, it enables decision-makers to identify the best solutions that balance the trade-offs among the objectives.

In MOGA, the process begins by initializing a population of potential solutions, referred to as individuals or chromosomes. These individuals are randomly generated, and the number

of individuals is predetermined. Each individual represents a possible solution to the problem at hand. Next, the fitness of each individual is evaluated based on the multiple objectives of the problem. This evaluation determines how well an individual performs with respect to the objectives. It is common for these objectives to conflict with each other, meaning that optimizing one objective may lead to the degradation of another. A selection process follows, where individuals are chosen from the population for the next generation based on their fitness values. The selection is typically designed to favor individuals who are closer to the Pareto-optimal front, which is promoted in the population.

After the selection process, genetic operators, such as crossover and mutation, are applied to generate offspring for the next generation. Crossover involves exchanging genetic information between two or more individuals to generate new solutions. Mutation introduces small random changes to the offspring, which help to explore new areas of the solution space.

The offspring then replace a portion of the existing population, maintaining a constant population size. This step promotes diversity within the population and enables further exploration of the solution space.

The algorithm continues to iterate through selection, crossover, mutation and replacement steps until a termination condition is met. This condition can be a predefined number of generations, a maximum computation time, or reaching a satisfactory level of convergence. At the end of the algorithm, the set of non-dominated individuals forms a Pareto-optimal front. These solutions cannot be improved upon in one objective without sacrificing another, which represents the best trade-offs between the conflicting objectives.

Finally, post-processing techniques can be applied to analyze and visualize the Pareto-optimal front, aiding decision-makers to understand the trade-offs and make informed choices.

3.2.3. Parameters of the MOGA. The parameters of the MOGA are values that define various aspects of the algorithm's behavior and influence its performance. The parameters of the MOGA used in this paper are mentioned in table 7.

Table 7. The parameters of the MOGA.

Parameter	Value
Constraint tolerance	1×10^{-3}
Creation	Uniform
Crossover function	Crossover intermediate
Crossover fraction	0.8
Elite count	0.05%
Function tolerance	1×10^{-4}
Max generations	800
Migration direction	Both
Migration fraction	0.2
Mutation function	Mutation adapt feasible
Pareto fraction	0.35
Penalty factor	100
Population size	100
Selection function	Tournament

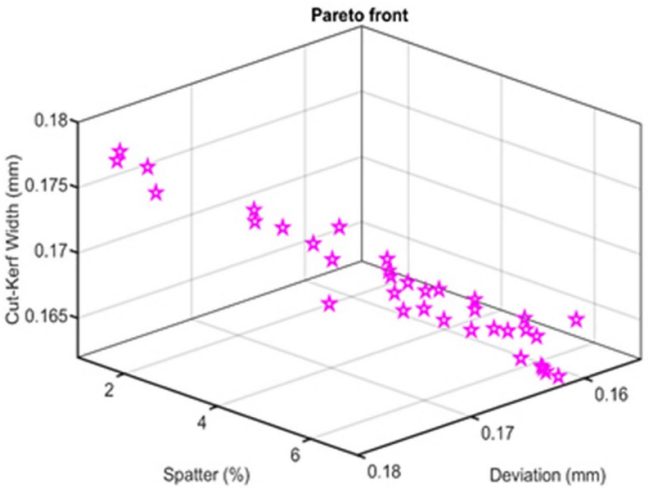

Figure 14. Pareto front.

3.2.4. Optimization results. In this paper, the objective functions are deviation, spatter and cut-kerf width. When dealing with three objective functions, the Pareto front is typically represented in a 3D space, with each axis corresponding to one of the objectives. The Pareto front itself consists of a collection of points, each representing a solution that achieves a particular trade-off between the three objectives. The goal is to simultaneously optimize all three objectives. The Pareto front consists of a set of solutions that achieve the best possible trade-offs among the objective functions. Each solution in the Pareto front represents a unique combination of values for the objective functions.

Visualizing the Pareto front in a 3D space can provide valuable insight into the trade-offs between the objectives. The Pareto front is illustrated in figure 14. It is important to note that the Pareto front contains multiple disconnected regions.

The average-spread graph is a visualization that provides insight into the spread or diversity of solutions along the Pareto front during the optimization process. It is commonly used as a performance metric to assess the convergence and diversity of the algorithm. The average-spread graph plots the average distance between adjacent solutions on the Pareto front as a function of the number of generations. The purpose of the average spread graph is to monitor how the solutions on the Pareto front are distributed in the objective space. The average-spread graph is shown in figure 15.

As can be seen, during the early stages of optimization, the spread is large, indicating a diverse set of solutions covering different regions of the Pareto front. As the algorithm progresses, the spread gradually decreases, reflecting convergence towards the true Pareto front. Finally, an average spread of 0.068 is achieved.

The optimal solutions of the Pareto front and the corresponding optimal decision parameters are shown in table 8. As can be seen, to minimize deviation, spatter and cut-kerf

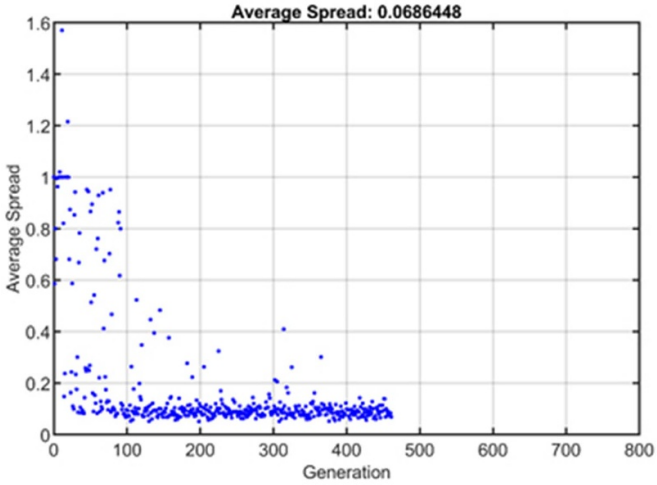

Figure 15. Average-spread graph.

Table 8. The optimal solutions of the Pareto front and the corresponding optimal decision parameters.

The optimal decision parameters				The optimal objective functions		
Power (w)	Speed (m min^{-1})	Focal distance (mm)	Pressure (bar)	Deviation (mm)	Spatter (%)	Cut-kerf width (mm)
610.3	11.8	0.0	8.0	0.162	6.115	0.165
649.5	12.4	0.0	7.3	0.169	2.823	0.171
613.8	11.7	0.0	8.0	0.161	6.135	0.164
655.8	11.4	0.0	7.6	0.171	4.209	0.167
636.3	12.1	0.0	7.8	0.164	4.514	0.167
627.3	12.2	0.0	7.9	0.162	5.113	0.166
621.6	12.0	0.0	7.7	0.163	4.625	0.167
629.5	11.6	0.0	7.6	0.166	4.371	0.167
641.5	11.7	0.0	7.8	0.167	4.855	0.167
635.1	11.6	0.0	7.8	0.164	5.003	0.165
609.3	11.1	0.0	8.0	0.162	6.689	0.163
647.6	12.2	0.0	7.4	0.168	3.130	0.170
634.5	12.2	0.0	7.6	0.165	4.063	0.168
651.2	12.3	0.0	7.1	0.170	2.464	0.172
652.2	12.2	0.0	7.2	0.171	2.611	0.172
684.5	12.7	0.0	6.6	0.179	1.714	0.178
620.6	12.0	0.0	7.5	0.165	3.892	0.169
612.9	11.6	0.0	7.9	0.162	5.781	0.165
637.8	12.1	0.0	7.7	0.165	4.087	0.168
618.5	11.4	0.0	7.8	0.164	5.452	0.165
614.4	11.3	0.0	7.9	0.163	6.270	0.163
678.2	12.4	0.0	7.0	0.177	1.994	0.175
630.4	12.0	0.0	7.7	0.164	4.258	0.167
616.5	12.1	0.0	7.2	0.167	3.377	0.171
686.2	12.7	0.0	6.7	0.180	1.728	0.178
617.5	11.6	0.0	7.9	0.162	5.615	0.165
615.2	11.8	0.0	7.8	0.162	5.233	0.166
682.7	12.6	0.0	6.8	0.177	1.774	0.177
610.8	11.2	0.0	8.0	0.162	6.522	0.163
621.5	11.4	0.0	7.7	0.165	4.858	0.166
608.6	12.0	0.0	7.9	0.161	5.976	0.166
651.7	12.3	0.0	7.6	0.168	3.515	0.169
609.0	11.1	0.0	8.0	0.161	6.807	0.162
609.7	11.2	0.0	8.0	0.162	6.608	0.163
605.2	12.2	0.0	8.0	0.158	6.312	0.165

width, it is desirable to use low power (from 605–685 W). Higher powers do not lead to optimal solutions. In addition, low speeds (in the range of 11.1–12.7 m min^{-1}) result in the best combinations of the decision parameters. The optimal focal distance is 0 mm for all solutions. Furthermore, a high pressure (between 6.5 and 8 bars) is more desirable to minimize the objective functions.

4. Conclusion

This study investigates the effect of laser cutting process parameters on dimensional tolerances and cut quality of holes in stainless-steel sheets through CCD and RSM. Furthermore, the process is optimized based on RSM regression models and a multi-objective genetic algorithm to systematically model and effectively optimize process parameters according to the experimental data.

- The ANOVA results show that the parameters of focal distance and laser power have had significant influence on deviation of hole diameter. The laser power is lower than 750 W and the cutting speed of about 13 m min^{-1} results in the minimum value of the deviation.
- By increasing the focal distance from 0.4 to 0.8 mm, the melt spattering rate has tripled.
- The focal distance and laser power have the greatest effect on the changes in the size of the cut kerf. Generally, narrow kerf width with smooth cutting edge surfaces produces a high-quality cut with fewer defects.
- The minimum deviation, spattering and cut-kerf width were achieved by using low power (from 605–685 W) and low speeds (in the range of 11.1–12.7 m min^{-1}) resulting in the best combinations of decision parameters. The optimal focal distance for all solutions is 0 mm. Higher pressure (between 6.5 and 8 bars) is desirable to minimize the objective functions.
- In future research, hole cutting at higher thicknesses up to 3 mm will be investigated. This study will focus on minimizing the geometrical tolerances of the hole diameter and taper angle. In addition, optimization of hole cutting in different aluminum alloys could be interesting due to possible industrial applications.

References

[1] Liu B and Lu W 2022 Surrogate models in machine learning for computational stochastic multi-scale modelling in composite materials design *Int. J. Hydromechatronics* **5** 336–65

[2] Gaur H, Khidhir B and Manchiryal R K 2022 Solution of structural mechanic's problems by machine learning *Int. J. Hydromechatronics* **5** 22–43

[3] Ahmad F 2022 Deep image retrieval using artificial neural network interpolation and indexing based on similarity measurement *CAAI Trans. Intell. Technol.* **7** 200–18

[4] Khan J, Lee E and Kim K 2022 A higher prediction accuracy–based alpha–beta filter algorithm using the feedforward artificial neural network *CAAI Trans. Intell. Technol.* **8** 1124–39

[5] Preethi P and Mamatha H R 2023 Region-based convolutional neural network for segmenting text in epigraphical images *Artif. Intell. Appl.* **1** 119–27

[6] Saminu S *et al* 2023 Applications of artificial intelligence in automatic detection of epileptic seizures using EEG signals: a review *Artif. Intell. Appl.* **1** 11–25

[7] Hebbi C and Mamatha H R 2023 Comprehensive dataset building and recognition of isolated handwritten kannada characters using machine learning models *Artif. Intell. Appl.* **1** 179–190

[8] Yongbin Y, Bagherzadeh S A, Azimy H, Akbari M and Karimipour A 2020 Comparison of the artificial neural network model prediction and the experimental results for cutting region temperature and surface roughness in laser cutting of AL6061T6 alloy *Infrared Phys. Technol.* **108** 103364

[9] Wang J, Sun Z, Gu L and Azimy H 2021 Investigating the effect of laser cutting parameters on the cut quality of Inconel 625 using response surface method (RSM) *Infrared Phys. Technol.* **118** 103866

[10] Pramanik D, Roy N, Kuar A S, Sarkar S and Mitra S 2022 Experimental investigation of sawing approach of low power fiber laser cutting of titanium alloy using particle swarm optimization technique *Opt. Laser Technol.* **147** 107613

[11] Deng C, Zhang L and Deng H 2022 Improving sentence simplification model with ordered neurons network *CAAI Trans. Intell. Technol.* **7** 268–77

[12] Wang L and Rong Y 2022 Review on processing stability, weld defects, finite element analysis, and field assisted welding of ultra-high-power laser ($\geqslant$ 10 kW) welding *Int. J. Hydromechatronics* **5** 167–90

[13] Sun C, Dehkordi M H R, Kholoud M J, Azimy H and Li Z 2023 Systematic evaluation of pulsed laser parameters effect on temperature distribution in dissimilar laser welding: a numerical simulation and artificial neural network *Opt. Laser Technol.* **163** 109407

[14] Li W, Rong Y, Huang Y, Chen L, Yang Z and Zhang G 2023 Effect of thermal damage on dynamic and static mechanical properties of CFRP short pulse laser hole cutting *Eng. Fract. Mech.* **286** 109306

[15] Alsoruji G, Muthuramalingam T, Moustafa E B and Elsheikh A 2022 Investigation and TGRA based optimization of laser beam drilling process during machining of Nickel Inconel 718 alloy *J. Mater. Res. Technol.* **18** 720–30

[16] Muthuramalingam T, Akash R, Krishnan S, Phan N H, Pi V N and Elsheikh A H 2021 Surface quality measures analysis and optimization on machining titanium alloy using CO_2 based laser beam drilling process *J. Manuf. Process.* **62** 1–6

[17] Chengal Reddy V, Keerthi T, Nishkala T and Maruthi Prasad Yadav G 2021 Analysis and optimization of laser drilling process during machining of AISI 303 material using grey relational analysis approach *SN Appl. Sci.* **3** 335

[18] Gopinath C, Lakshmanan P and Palani S 2022 Fiber laser microcutting on duplex steel: parameter optimization by TOPSIS *Mater. Manuf. Process.* **37** 985–94

[19] Chatterjee S, Mahapatra S S, Bharadwaj V, Upadhyay B N and Bindra K S 2021 Prediction of quality characteristics of laser drilled holes using artificial intelligence techniques *Eng. Comput.* **37** 1181–204

[20] Pramanik D, Kuar A S, Sarkar S and Mitra S 2021 Optimisation of edge quality on stainless steel 316L using low power fibre laser beam machining *Adv. Mater. Process. Technol.* **7** 42–53

[21] Xia K, Wang H, Ren N, Ren X, Liu D, Shi C, Li T and Tian J 2021 Laser drilling in nickel super-alloy sheets with and without ultrasonic assistance characterized by transient in-process detection with indirect characterization after hole-drilling *Opt. Laser Technol.* **134** 106559
[22] Wang H, Xu Y, Liu J, Hu Q, Wang X, Ren N, Zhou W and Ren X 2021 Magnet-assisted laser hole-cutting in magnesium alloys with and without water immersion *J. Manuf. Process.* **61** 539–60
[23] Hüseyin U, Meral T and Günay M 2020 Modelling and optimization of burr height in fiber laser drilling of ferritic stainless steel *Imalat Teknolojileri ve Uygulamalari* **1** 32–39
[24] Wang R, Dong X, Wang K, Sun X, Fan Z and Duan W 2019 Two-step approach to improving the quality of laser micro-hole drilling on thermal barrier coated nickel base alloys *Opt. Lasers Eng.* **121** 406–15
[25] Amaral I, Silva F J G, Pinto G F L, Campilho R D S G and Gouveia R M 2019 Improving the cut surface quality by optimizing parameters in the fibre laser cutting process *Proc. Manuf.* **38** 1111–20
[26] Mustafa A Y 2018 Modelling of the hole quality characteristics by extreme learning machine in fiber laser drilling of Ti-6Al-4V *J. Manuf. Process.* **36** 138–48
[27] Moradi M and Golchin E 2017 Investigation on the effects of process parameters on laser percussion drilling using finite element methodology; statistical modelling and optimization *Latin Am. J. Solids Struct.* **14** 464–84